





PointCompress3D: A Point Cloud Compression Framework for Roadside LiDARs in Intelligent Transportation Systems

Walter Zimmer ✉ ★ 

Ramandika Pranamulia ★ 

Xingcheng Zhou 

Mingyu Liu 

Alois C. Knoll 

Technical University of Munich

<https://pointcompress3d.github.io>

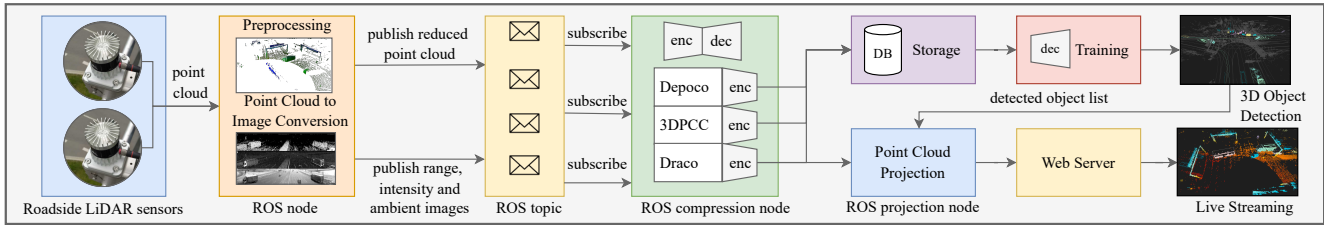


Figure 1. **Visualization of the processing pipeline of our *PointCompress3D* point cloud compression and streaming framework.** Our framework takes raw roadside LiDAR point clouds as input, processes them, and outputs compressed point clouds to facilitate downstream application tasks like 3D object detection, data storage, and real-time point cloud streaming on an ITS test bed for autonomous driving.

Abstract

In the context of Intelligent Transportation Systems (ITS), efficient data compression is crucial for managing large-scale point cloud data acquired by roadside LiDAR sensors. The demand for efficient storage, streaming, and real-time object detection capabilities for point cloud data is substantial. This work introduces *PointCompress3D*, a novel point cloud compression framework explicitly tailored for roadside LiDARs. Our framework addresses the challenges of compressing high-resolution point clouds in real time while maintaining accuracy and compatibility with roadside LiDAR sensors. We adapt, extend, and integrate three cutting-edge compression methods and evaluate them on the real-world TUM Traffic datasets. Moreover, we deploy our compression framework on a real ITS test bed for autonomous driving and test it under real traffic conditions. After fine-tuning, we achieve a frame rate of 10 FPS while keeping compression sizes below 105 Kb, a reduction of 50 times, and maintaining object detection performance on par with the original data. In extensive experiments and ablation studies, we finally achieved a PSNR d2 of 94.46 and a BPP of 6.54 on the TUM Traffic datasets. The code is available on our project website.

1. Introduction

This work is carried out within a project that contributes significantly to various aspects of improving mobility in transportation systems, including the creation of a live digital twin of the traffic to facilitate automated driving on level 4. One concept for developing ITS systems to create live digital twins of the traffic involves the installation of cameras and LiDAR sensors at the sides of roads and junctions. These sensors capture data from the traffic, which is then fused, and disseminated to all entities who have subscribed to the live digital twin of the traffic. LiDAR sensors employ laser light for distance measurement, translate the environment into a collection of 3D points, and facilitate the creation of precise three-dimensional digital twins of the surroundings. These high-resolution sensors operate at 10-30 Hz and emit up to 2.6 Mio. points per second (pps). This results in a significant amount of data, ranging from 5-25 MB per frame. There are many use cases for roadside infrastructure LiDAR sensors. One of the most crucial tasks is to process point cloud data to detect traffic participants. Numerous scene understanding [42] and object detection methods [44, 46, 47, 50] have been developed for that purpose, using, e.g., *PointPillars* [21] as their baseline. In other cases, they can be incorporated with multiple input sources like images to perform multi-modal object detection [14, 16, 23, 26]. However, the large amount of

✉ Corresponding author: walter.zimmer@tum.de

★ These authors contributed equally.

Method	Year	BPP↓	PSNR (d1) [db]↑	PSNR (d2) [db]↑	Enc. Speed [ms]↓	Dec. Speed [ms]↓	Code	Dataset
MPEG-GPCC [34]	2018	1.00 [10]	67.00 [10]	73.00 [10]	160.20 [6]	112.80 [6]	✓	SemanticKITTI
Draco [12]	2018	5.98 [15]	–	44.19 [15]	25.80 [6]	15.30 [6]	✓	–
OctSqueeze [18]	2020	1.00 [10]	69.00 [10]	74.00 [10]	35.75	92.96	✓	SemanticKITTI
MuSCLC [6]	2020	5.00	–	<u>81.00</u>	20.80	49.00	–	SemanticKITTI
VoxelContext-Net [32]	2021	1.00 [10]	<u>72.00</u> [10]	76.00 [10]	388.90 [†] [10]	374.10 [†] [10]	–	SemanticKITTI
Depoco [39]	2021	4.98 [15]	–	40.01 [15]	32.00 [15]	2.00 [15]	✓	SemanticKITTI
OctAttention [11]	2022	1.00 [10]	73.00 [10]	77.00 [10]	2.30 [‡] [10]	2060.2 [‡] [10]	✓	SemanticKITTI
GrASPN [30]	2022	1.00	53.00	57.00	193.80	345.92	✓	Ford
RIDDLE [43]	2022	5.00	–	95.00	532.51	966.30	–	SemanticKITTI
D-PCC [15]	2022	4.23	–	47.98	80.00	24.00	✓	SemanticKITTI
3DPCC [4]	2022	10.00	–	–	35.00*	<u>5.00</u> *	✓	–
OctFormer [10]	2023	1.00	<u>72.00</u>	76.00	<u>5.20</u>	7.30	✓	SemanticKITTI
InterFrame [3]	2024	0.06	70.10	73.00	364.00	714.00	–	8iVFB v2

[†]Using a voxel size of 5.

[‡]Using a context window size of N=1024.

*Using JPEG2000 compression instead of RNN.

Table 1. **Performance evaluation of state-of-the-art point cloud compression methods.** We report the *BPP* metric for *PSNR* d2 and highlight the supported methods in gray. Best results are marked in bold, second best are underlined.

data poses challenges to processing, storing, and transmitting these point clouds.

Our contribution is the following:

- We propose a point cloud compression framework shown in Fig. 1 for roadside infrastructure LiDARs.
- We provide an in-depth comparison and analysis of state-of-the-art compression methods on *SemanticKITTI* [5], *Ford* [2] and the *TUM Traffic* datasets [8, 9, 45, 49].
- We extend existing compression methods to make them compatible with our roadside LiDAR sensors.
- We perform extensive experiments and ablation studies on the *TUMTraF Intersection* and *TUMTraF V2X Cooperative Perception* dataset and achieve a *PSNR* d2 of 94.46 and a *BPP* of 6.54.
- We open-source the code of our framework, which contains the point cloud projection and compression module, and provide a website with video results.

2. Related Work

Point cloud data consists of (x, y, z) geometric coordinates and can also contain additional attributes based on the manufacturer, such as intensity, reflectivity, time, ambient, ring, and range. Moreover, attributes such as RGB colors or normals can be added to the point clouds. However, most point cloud compression methods focus only on geometry compression. Methods compressing attributes in addition to geometry do both compressions separately. Geometry compression is highly prioritized because it is still difficult to get a good balance of fast compression speed, low bit rate, and low reconstruction error.

2.1. Geometry compression

The focus is on compressing 3D coordinates, representing geometrical shapes, with various techniques. The first step usually involves converting 3D coordinates into a dense representation, such as tree structures [12, 34], voxels [29, 32], or 2D images [4, 17]. After obtaining this dense representation, various methods can be applied depending on the previously chosen structure. In general, the processing methods will exploit the statistical properties of the data using hand-crafted or learning-based methods.

2.2. Octree representation

We can encode the *octree*'s occupancy nodes using predictive and arithmetic coding for the *octree* representation. Predictive coding is used to predict the occupancy symbol of the *octree* nodes based on their neighbors. This can be achieved by hand-crafted entropy models [34] or by using deep learning-based methods to automatically learn the entropy model [11, 18, 36]. Arithmetic coding is mostly used to encode the residual error from comparing the original data to the reconstructed data [31]. Unfortunately, this approach is highly complex when dealing with large point cloud data since constructing the *octree* and performing traversal operations can be time-consuming. A precision loss might also be part of the *octree*-based codec because of the quantization process that took place. We might minimize *octree* complexity and the precision loss by limiting the *octree* depth and using a less aggressive quantization level, respectively. Still, it results in a lower compression ratio.

2.3. Voxelization

Voxelizing the point cloud into 3D structural grids with specified grid sizes as shown in Algorithm 1 is another common representation. This extends the concept of 2D images constructed by pixels, while in this case, the 3D space is

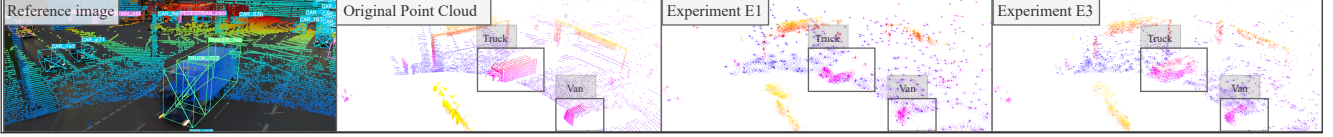


Figure 2. **Visualization of ablation study results for *Depoco* on the *TUMTraF V2X Cooperative Perception* [49] dataset.** From left to right: a) Reference image b) View of the original point cloud. b) Experiment E1: Reconstructed point cloud with a subsampling distance of 3.0 and a minimum kernel radius of 1.5. c) Experiment E3: Reconstructed point cloud with a subsampling distance of 1.0 and a minimum kernel radius of 1.2. Both reconstructed point clouds are generated with max. 30,000 points and a grid size of 40x40x15 m.

Algorithm 1 Voxelization Process

- 1: **Input:** Point cloud data \mathcal{P} , Voxel size v
 - 2: **Output:** Voxel grid representation \mathcal{V}
 - 3:
 - 4: **Procedure:**
 - 5: Define the resolution of the voxel grid by specifying the voxel size v .
 - 6: Divide the 3D space occupied by the point cloud \mathcal{P} into a regular grid of voxels.
 - 7: **for** each voxel $voxel$ in \mathcal{V} **do**
 - 8: Initialize voxel values based on assignment method:
 - 9: **Binary occupancy:** Set voxel value to 1 if it contains one or more points, 0 otherwise.
 - 10: **Averaged properties:** Calculate average properties (e.g., intensity, range) of points within voxel.
 - 11: **Density:** Count the number of points within the voxel and store them as a value.
 - 12: **end for**
-

made of *voxels*. This aims to bring the concepts of 2D processing into 3D space, one of which is a *3D CNN autoencoder* that we can employ to compress those *voxels* through the encoder part and decompress them through the decoder part [32]. Another method we can apply to those *voxel* representations is masked convolutions to predict *voxel* occupancy probabilities sequentially, feeding previously predicted *voxels* as context [27], which is inspired by combining *voxels* and the *octree* representation. This voxelization method has a similar problem to that of *octree* methods, where the size of the *voxels* will affect the compression speed.

2.4. 3D Transformation

As for projection transformation, where the transformation results are images, compression technology for images has advanced significantly. Hence, we can utilize available technologies such as *JPEG* or deep learning-based image compression [37] methods to get a good compression result like in [4]. The advantage of this method is that the transformation directly reduces the size without the compression process. Each 3D point represented as (x, y, z) gets reduced to a single variable representing the range of the point from

the observation source. Beemelmanns et al. [4] achieve a lossless compression and precisely reconstruct the original point. Nevertheless, this approach is limited to a specific scenario in that no 3D point is occluded by another point. Merged point clouds from multiple LiDARs cannot be reconstructed this way. It also relies on the projection parameters, such as the position of the sensor and the azimuth angles, which are specific to the LiDAR type and manufacturer. Moving the sensor will require a recalibration of the LiDAR.

3. Methodology

We first compare 13 available state-of-the-art methods and analyze their performance based on the BPP and PSNR metrics, as well as the encoding and decoding speed. Then, we choose the best three state-of-the-art compression algorithms (*Depoco*, *3DPCC*, and *Draco*) and adapt them to make them compatible with the *TUMTraF* datasets [24] and the Ouster LiDAR sensor. Furthermore, we extend these algorithms and fine-tune the parameters to find the best trade-off between compression ratio and speed and improve the compression quality. Finally, we integrate them into our *PointCompress3D* compression and streaming framework and connect them to a LiDAR 3D object detector to stream compressed point clouds with detected 3D objects.

3.1. Method Selection

To choose the most promising method from the state of the art, we first evaluate and inspect various aspects of each method, such as compression efficiency, compression effectiveness, compression speed, and code availability (see Table 1). The bitrate indicates the number of bits required per data point in a point cloud. Factors like spatial information and additional data stored influence it. Each bitrate corresponds to a unique *Peak Signal-to-Noise Ratio (PSNR)* value. Still, variations in the *PSNR* formula, particularly the *MAX* parameter, can affect comparisons between methods.

The strategies employed to ensure comparability between methods include:

- We only focus on geometry compression, i.e., spatial attributes.

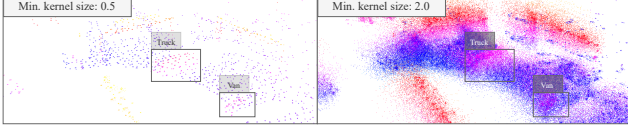


Figure 3. **Ablation study results for *Depoco*:** Adjusting the *minimum kernel radius* parameters by 0.5 times and 2 times the original value, respectively.

- As *SemanticKITTI* is the most widely used dataset for point cloud compression, we focus on gathering methods evaluated on this dataset.
- We only consider methods that use 1 or 5 *BPP* for each *PSNR* value evaluation.
- When the performance of a given method is not given, we refer to the related work that states the desired metric to provide cross-sourced metric findings.
- We only consider *bits per point* as required to encode spatial attributes.

Looking at Table 1, with priority given to speed and code availability before reconstruction error, we find four promising methods that run under 10 FPS. Although *MuS-CLE* [6] fulfills the speed requirement, the code is not publicly available. Of all four candidates, *Depoco* is the fastest one, followed by *Draco*, with their total encoding and decoding speed being 34 ms and 40 ms, respectively. *Depoco*'s and *Draco*'s reconstruction errors are also comparable and not significantly different. Hence, we evaluate both *Draco* and *Depoco* alongside another additional method, *3DPCC-RNN* [4], on our dataset. *3DPCC-RNN* converts 3D point clouds to range images and vice versa. This enables us to utilize image compression algorithms, which are more advanced and promising than directly compressing the 3D point cloud.

3.2. Extensions

We extend and modify three point cloud compression algorithms to make them compatible with roadside LiDAR sensors and improve their compression quality and speed.

Depoco. *Depoco* is a learning-based compression method using autoencoders [39]. Configuration files and pre-trained weights of the *Depoco* model are provided. Using grid search, we tune the parameters listed in Tab. 2 and start from the configuration file with the best qualitative result. Figure 2 shows how the initial configuration performs on the *TUMTraF Intersection* dataset. We can see that the configuration with a subsampling distance of 1.0 and a minimum kernel radius of 1.2 performs best. Both compressed images are generated with max. 30,000 points and a grid size of [40, 40, 15] m. The truck and the car look almost

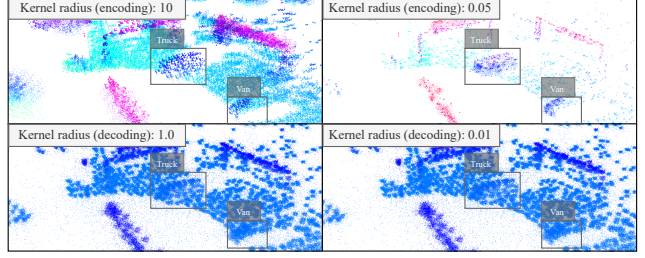


Figure 4. **Ablation study results for *Depoco*:** We set the *kernel radius* in encoding block to 10 and 0.05 (top row) while keeping the decoding block values constant at 0.05. Subsequently, we set *kernel radius* in the decoding block to 1 and 0.01 (bottom row) while keeping the encoding block values constant at 1.0.

identical as in the original point cloud frame. The mean encoding time for experiment E1 is 64 - 65 ms, and for experiment E3 is 110 - 120 ms, while the mean decoding time for both configurations is 90 ms. Therefore, we opted to start tuning from configuration E3, prioritizing encoding speed within the 0.1 s limit while ensuring superior quality performance.

We begin by tuning the following parameters: *subsampling distance*, *min. kernel radius*, and *kernel radius*. To maintain compatibility with the provided pre-trained weights, we retain the original *subsampling distance*. Adjustments to this parameter were found to cause block dimension mismatches. Thus, it remains unchanged to utilize the existing weights effectively.

Next, we adjust the *min. kernel radius* parameter. The result is depicted in Figure 3. We observe that enlarging the variable results in denser points while reducing it decreases the number of points. However, our current value appears optimal, as the object boundaries are well-defined and perceivable. Moving on, we tune the *kernel radius* in encoder and decoder blocks, with the default settings being 1.0 for the encoder and 0.05 for the decoder. Once again, examining the results in Figure 4, we find that the original parameter yields the best result. Subsequently, we adjust the *max. number of points*, similar to the *min. kernel radius* and *kernel radius*. Notably, for *max. number of points*, the points added to the scene are around the dynamic objects, where the object remains perceptible but becomes densely populated with points, lacking inner details shown in Figure 5. We do not inspect the *grid feature dimension* because the grid size is the tile unit where compression is applied. This implies that smaller grid sizes should result in better compression quality. Moreover, the *grid feature dimension* does not affect the reconstruction quality. It is only modified if additional attributes, such as the intensity, need to be encoded.

3DPCC. In [4], Beemelmans *et al.* present a novel approach for a lossless and calibrated 3D-to-2D transforma-

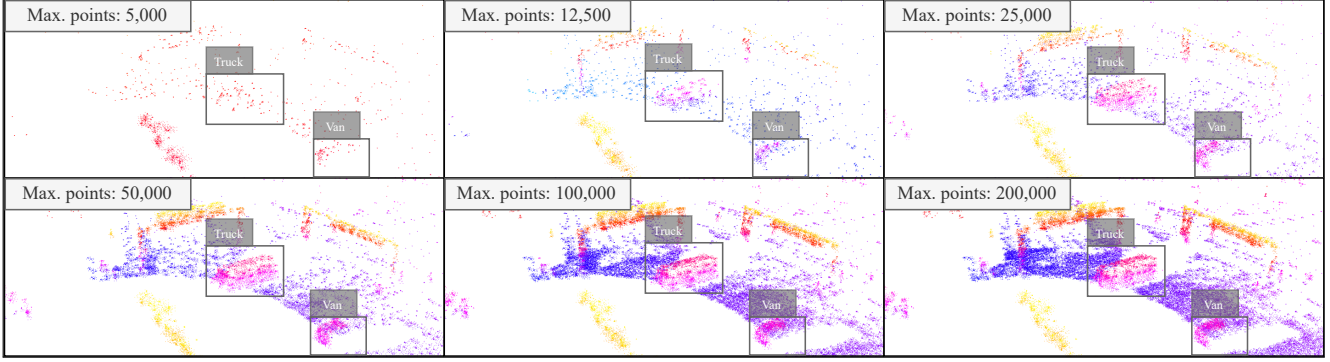


Figure 5. **Visualization of the ablation study results for *Depoco* for the max. number of points.** The point cloud shows a side view of a truck and a car with 5,000, 12,500, 25,000, 50,000, 100,000, and 200,000 points.

tion which allows compression algorithms to efficiently exploit spatial correlations within the 2D representation. The authors employ *JPEG2000*, *PNG*, and *RNN*-based compression methods [37] to compress the images. We use *Ouster* LiDAR sensors, which require specific modifications due to differences in settings compared to *Velodyne* LiDARs.

It’s important to note that *Velodyne*’s point cloud data does not come with range images, necessitating a conversion algorithm. In contrast, *Ouster* LiDARs provide range images alongside point cloud data. However, without azimuth maps, we are restricted to using the built-in range images directly. In some experiments, we replaced the point cloud-transformed range image with the built-in range image for the reconstruction, as seen in Tables 3 and 4.

The *3DPCC* compression framework is integrated into a *ROS* system. Communication occurs through *ROS* topics and messages. To utilize point clouds from *Ouster* LiDARs, we had to convert them into the correct point cloud data format. Three images representing one point cloud frame are produced: the range, intensity, and azimuth images. To convert them back to the point cloud structure, we perform a 2D to 3D transformation.

Next, we adjust the azimuth and elevation angles in the configuration file because the *Ouster* LiDAR mounted on our roadside infrastructure has a below-horizon beam configuration. *Velodyne* LiDAR sensors used in [4] have 32 beams, 16 above the horizon and 16 below. Our *Ouster* LiDAR sensors have 64 beams, all set up to point below the horizon. We also need to order the elevation angle from lower to higher, and the azimuth angle should correspond to the right elevation angle representing a configuration of a laser beam.

In the last step, we modify the input point cloud. The initial order of points is sorted based on width, which is 2048 in our case. Therefore, the first 2048 rows correspond to one LiDAR beam closest to the horizon. The next 2048

rows correspond to the second LiDAR beam closest to the horizon. This is equivalent to all 64 beams. Hence, we have $2048 * 64 = 131,072$ points in a single point cloud scan. We change the order of the points to columns: The first column represents the different 64 LiDAR scans, and the second column represents another 64 LiDAR scans, up to 2048 columns scanned.

Draco. To use the *Draco* point cloud compression method in our framework, we integrate the *DracoPy* Python bindings [20], which wrap the *Draco* executables. We optimize the quantization bits and compression level parameters specifically for *Ouster* LiDAR data. By fine-tuning these parameters using grid search, we ensured an efficient and effective compression of point clouds generated from *Ouster* LiDARs to decrease the file storage size and improve transmission bandwidth for LiDAR-based applications.

4. Evaluation

To gain more insights into the performance of the selected compression methods, we perform several experiments and ablation studies on the *TUMTraF Intersection* and the *TUMTraF V2X Cooperative Perception* dataset.

4.1. Performance Metrics

In compression, we encounter diverse metrics assessing performance and quality. We balance speed, quality, and performance and determine the best trade-off. We assess the reconstruction quality at specific compression rates, comparing metric graphs to determine method superiority.

PSNR. Following [19] based on [34], we use *PSNR* (Peak Signal-to-Noise Ratio) with the *d1* and *d2* metric, as reconstruction metric. *PSNR* is a widely used metric in image and video compression to evaluate the quality of the compressed image or video compared to the original ones. It measures the reconstruction quality in both directions by comparing the *mean squared error* (MSE) between the orig-

Grid Size	Max. Points	Enc. (ms)↓	Dec. (ms)↓	Enc. VRAM (GB)↓	Dec. VRAM (GB)↓	PSNR d1↑	PSNR (d2)↑	BPP↓	mAP _{3D} ↑
8x8x3	50,000	220	2.7	3.9	3.9	15.32	23.68	7.48	13.32
	100,000	410	2.7	6.0	4.3	21.81	30.13	11.72	17.29
	200,000	520	2.8	5.5	7.1	24.18	32.88	13.57	19.39
16x16x6	50,000	230	2.6	3.0	2.7	-7.81	-0.19	5.17	12.21
	100,000	350	2.5	4.3	3.7	-3.59	3.87	7.03	19.50
	200,000	510	2.7	6.8	4.0	-1.46	6.31	7.73	20.91
24x24x9	50,000	240	2.5	2.2	2.7	-5.57	0.99	3.90	13.59
	100,000	410	2.6	5.5	3.1	-1.87	5.50	4.94	19.75
	200,000	530	2.7	6.6	3.2	-0.18	7.47	5.31	19.32

Table 2. **Parameter tuning results for Depoco on the max. number of points and the grid size.** We use the *TUMTraf Intersection* dataset to find the best parameters and evaluate the compression method on the *TUMTraf V2X Cooperative Perception* dataset.

inal and compressed point cloud (see Eq. (1)). The PSNRs of the two directions are then combined to obtain a single symmetric PSNR value with the maximum pooling function, as defined in Eq. (2).

$$\text{PSNR}_{A,B} = 10 \cdot \log_{10} \left(\frac{p_s^2}{d_{A,B}^{MSE}} \right) \quad (1)$$

$$\text{PSNR} = \max(\text{PSNR}_{A,B}, \text{PSNR}_{B,A}) \quad (2)$$

where p is the signal peak d is the average squared error (i.e. MSE) between all point in point cloud A and their corresponding neighbor in point cloud B. *PSNR* is measured in decibels (dB), and a higher *PSNR* value indicates better quality because the *MSE* is smaller. In the case of point clouds, the *MAX* value can be set in various ways, depending on the compression type, such as voxelized or not [19]. The most common method is to set it to the value of the maximum diagonal of the box bounding of the point cloud.

Chamfer Distance. It's similar to *PSNR* in terms of a measurement system for reconstruction error. The *Chamfer* distance between two point clouds $P_1 = \{x_i \in \mathbb{R}^3\}_{i=1}^n$

and $P_2 = \{x_j \in \mathbb{R}^3\}_{j=1}^m$ is defined as the average distance between pairs of nearest neighbors between P_1 and P_2 i.e.

$$C(P_1, P_2) = \frac{1}{2n} \sum_{i=1}^n |x_i - \text{NN}(x_i, P_2)| + \frac{1}{2m} \sum_{j=1}^m |x_j - \text{NN}(x_j, P_1)| \quad (3)$$

where $\text{NN}(x, P) = \arg\min_{x' \in P} \|x - x'\|$ is the nearest neighbor function and n, m are the number of points in P_1, P_2 respectively. The *Chamfer* distance has a minimum of 0, meaning that two sets are spatially identical. We can also adjust the distance metric $\|\cdot\|$ with various distance metrics such as *Manhattan* or *Euclidian* distance metric.

Bits per point. Compression rate is measured using *bits per point (BPP)*, indicating the bits needed to store a single point. For instance, a binary *pcd* file with 16-bit precision for (x, y, z) coordinates requires $3 \times 16 = 48$ bits, which equals 6 bytes. In contrast, *ASCII* format uses 3-36 bytes due to its readable text storage (1 byte per character). Compression formats achieve significantly smaller sizes.

Metric Graph. For each *bits per point* value representing compression method efficiency, there will be a *PSNR* value indicating the reconstruction quality of that specific *BPP* from a certain compression method (see Tab. 1). We can control *BPP* indirectly in several ways, including quantization level, *octree* depth, or entropy coding efficiency. This will also indirectly affect the *PSNR* value. It is important to note that the *BPP* value is proportional to *PSNR*. When the *BPP* value is higher, *PSNR* will also be higher and vice versa. Therefore, we usually use a 2D graph to map the efficiency and effectiveness of compression methods and compare their performance using those graphs.

Compression Speed. We also measure the compression and decompression speed individually to evaluate the performance of the methods. The speed is calculated only for compression and decompression processes, neglecting the speed required for pre- or postprocessing steps.

Memory Consumption. Finally, we report the allo-

Input Image	Size (gen.)	Size (orig.)	TinyJPG	PNG	ImgMagic
Range image	113.70	43.50	13.40	111.70	92.10
Azimuth image	56.30	-	10.20	65.30	56.30
Intensity image	20.72	-	6.20	21.90	20.72
Total Size (KB)	190.70	120.50	29.80	204.90	169.10

Table 3. **Results of the point cloud image (range, azimuth, and intensity) compression of 3DPCC on the TUMTraf-I dataset.** Size is given in KB.

Input Representation	PSNR d1	PSNR d2	mAP@50
Generated RIA [†]	25.93	36.23	7.49
Generated IA + Ori. R [†]	21.57	24.87	0.00
Generated IA + Comp. R [†] (ImageMagick)	26.38	33.72	2.48
Comp. RIA [†] (TinyJPEG)	26.10	26.92	0.04

[†] A=azimuth, I=intensity, R= range image.

Table 4. **Evaluation of the 3DPCC compression and the PointPillars 3D object detection performance on the TUMTraf-I dataset.** We compare four different input representations.

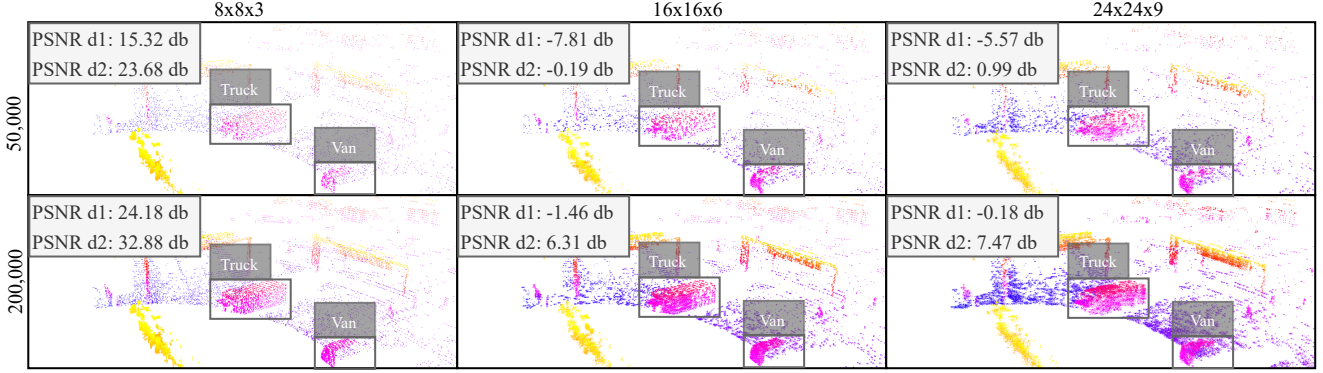


Figure 6. **Visualization of the ablation study results for Depoco.** We show the reconstructed point clouds for different grid sizes (x-axis) and point sizes (y-axis) on the *TUMTraF V2X Cooperative Perception* [49] dataset and report the PSNR d1 and d2 metrics.

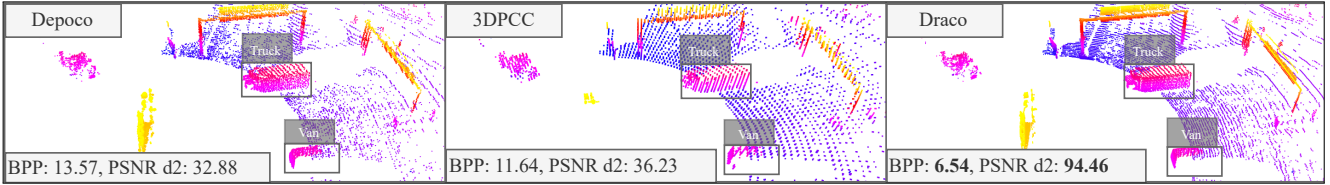


Figure 7. **Qualitative reconstruction results.** Qualitative comparison of *Depoco*, *3DPCC* and *Draco* on the *TUMTraF V2X Cooperative Perception* [49] dataset. *Draco* outperforms *Depoco* and *3DPCC* regarding the BPP and PSNR d2 metrics.

cated memory for the encoding and decoding on the GPU (VRAM) for each compression algorithm.

Mean Average Precision. The *mean average precision* (mAP) metric quantifies the average precision scores across multiple object categories, evaluating a detection model’s performance across different classes.

4.2. Experiment Setup

Datasets. We use the *TUMTraF Intersection* [45] (release R02, sequence S02) and the *TUMTraF V2X Cooperative Perception* [49] datasets, labeled with 3D BAT [48, 49], for our experiments. The latter one contains ten 10 s long sequences. Each sequence has 100 LiDAR point cloud scans and their corresponding 2D projection images (range, reflectivity, signal, near-infrared).

Hardware Setup. Our framework runs inside a docker container under an Ubuntu operating system. We use 3x NVIDIA GeForce RTX 3090 GPUs for our experiments, each having 24576 MiB of VRAM.

4.3. Quantitative Results

In this section, we evaluate different methods on the *TUMTraF datasets* and provide quantitative results for *bits per point*, *PSNR d1* and *d2*, encoding and decoding speed.

We find that the *max. number of points* and *grid size* are the most impactful parameters for Depoco. We present the results of our parameter fine-tuning in Table 2. The decod-

ing speed remains consistent across configurations, while the encoding speed, GPU memory usage, and BPP increase with a higher max. number of points. We calculate the BPP by dividing the encoded binary file size by the number of points in the original point cloud. We proceed by analyzing the conversion of 3D point clouds to 2D images. Each 3D point cloud frame yields three images (AIR): azimuth, intensity, and range. An example result is shown in Fig. 10. The transformation speed from 3D to 2D points is 300 ms, and from 2D to 3D points is 19 ms, while the *ImageMagick* PNG to JPG conversion takes approximately 15 ms. The average size of the range, azimuth, and intensity images from conversion compared to the original ones can be seen in Tab. 3. Further, we compress the images using *PNG* compression using the *PIL* python library, online compression *TinyJPG* [1], and *ImageMagick* library with compression level 100 for the range image only. As we can see from the table, the *PNG* compression by *PIL* hardly compresses the images followed by the *ImageMagick*, while the *TinyJPG* performs really well. At last, we evaluate the *Draco* method on the *TUMTraF-I* dataset, achieving encoding and decoding times of 60 ms and 80 ms, a PSNR of 52 dB and 144 dB, and an mAP of 20.01 and 20.11, respectively. Finally, we compare *Depoco*’s performance to *3DPCC* and *Draco*, visualizing it in a 2D graph (see Fig. 8).

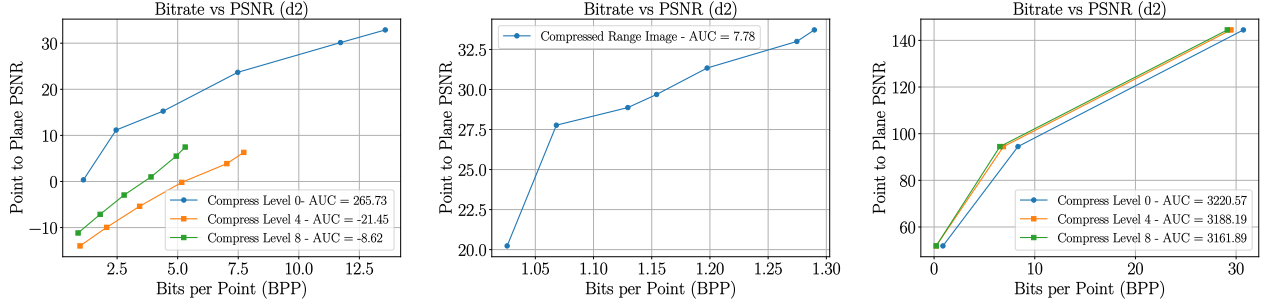


Figure 8. **Visualization of BPP and PSNR metrics.** From left to right: *Depoco*, *3DPCC* and *Draco*. We calculate the Area Under the Curve (AUC) metric for different compression levels and see that *Draco* outperforms the other methods.

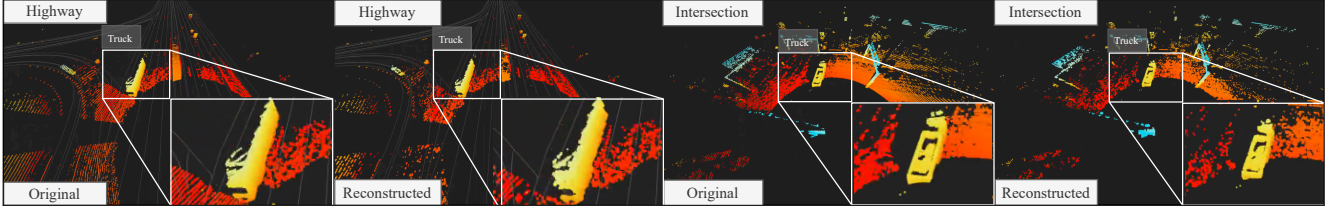


Figure 9. **Qualitative reconstruction results of *Depoco*.** Left to right: 1) Original and reconstructed point cloud of the TUM Traffic A9 Highway (TUMTraF-A9) dataset [8]. 2) Original and reconstructed point cloud of the TUM Traffic Intersection (TUMTraF-I) dataset [45].



Figure 10. **Results of the 3D to 2D transformation.** From top to bottom: range, azimuth, and intensity image. We post-process the images and show the front part of the LiDAR.

4.4. Qualitative Results

In Fig. 6 we show the reconstruction results for different parameters of *Depoco* that were fine-tuned and listed in Tab. 2. We illustrate how the *PSNR* value correlated to the grid size and the number of points. Increasing the *max. number of points* parameter will add more points to the scene after decoding and lead to a higher *PSNR* value. Note that we keep the grid size low, either $8 \times 8 \times 3$ or $16 \times 16 \times 6$, to get a good reconstruction result. Otherwise, reconstructed objects are blurry, as we can see in the $200k | 24 \times 24 \times 9$ setting, and it will get even more blurry as the grid size gets larger. Keeping the grid size small keeps the *PSNR* high, meaning that the reconstructed point cloud looks more similar to the original one. Fig. 7 illustrates the optimal reconstruction quality achieved at minimal bits per pixel for *Depoco*, *3DPCC*, and *Draco*. Finally, we show qualitative reconstruction results of *Depoco* on the *TUMTraF-A9* and the *TUMTraF-I* dataset (see Fig. 9).

5. Conclusion and Future Work

Draco emerges as the most promising method, with encoding and decoding speeds exceeding 10 FPS alongside good *PSNR* and *mAP* values. *Draco*'s *PSNR* and *mAP* values consistently correlate, with higher *PSNR* values leading to better *mAP* values. Quantization bits are revealed as the most influential parameters in *Draco*, with values of 16 yielding *mAP* values of 20.01 and 20.11 when set to the maximum of 30 bits. On the other hand, *Depoco* faces speed issues despite configurations surpassing the baseline *mAP* of 20.11. The surpassing result is due to *Depoco*'s introduction of additional points, enhancing object recognition but leading to inconsistent *PSNR*-*mAP* relationships. Lastly, *3DPCC* exhibits a good *PSNR d2* value of 36.23 compared to 32.88 for *Depoco* on the *TUMTraF-I* dataset. On the other hand, reconstructed point clouds with *3DPCC* lead to a very low 3D object detection performance (*mAP* of 7.49). We found that fixing the transformation to prevent loss of point clouds can improve that. Future work includes deploying our framework on the live system, and the extension to other LiDAR types and manufacturers.

Acknowledgment

This research was supported by the Federal Ministry of Education and Research in Germany within the project *AUTOtech.agil*, Grant Number: 01IS22088U.

Supplementary Material

<https://pointcompress3d.github.io/>

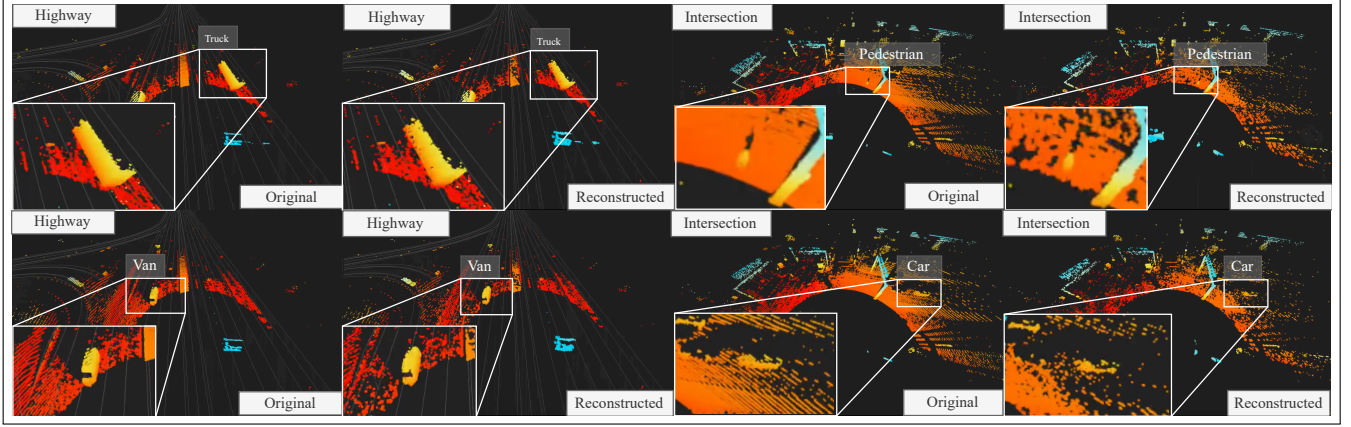


Figure 11. **Visualization of point cloud reconstruction results.** We show further reconstruction results of *Depoco* on the *TUMTraf-A9* and *TUMTraf-I* dataset. First row from left to right: 1) Original and reconstructed point cloud on the A9 Highway showing a truck, 2) Original and reconstructed point cloud at an intersection showing a pedestrian. Second row from left to right: 3) Original and reconstructed point cloud on the A9 Highway showing a van, 4) Original and reconstructed point cloud at an intersection showing a car.

Contents

A Task definition	9
B Further related work	9
B.1. Traditional point cloud compression	9
B.2. Learning based compression	10
C Implementation details	10
C.1. Hardware and software setup	10
C.2. Parameter tuning	10
D Point Cloud Compression Datasets	10
E Metrics	10
E.1. Performance metrics	10
E.2. Quality metrics	10
F Detailed visualization results	11
G Failure cases and limitations	11
G.1. Failure cases	11
G.2. Limitations	11

A. Task definition

Point cloud compression involves reducing the data size of point clouds, represented as sets of points $\{(x_i, y_i, z_i)\}$ in space, while preserving their geometric and attribute information. The task aims to minimize the storage S and

transmission time t requirements by finding a compact representation C such that $|C| \ll |P|$, where P denotes the original point cloud data. The goal of efficient compression algorithms is to achieve high compression rates $r = \frac{|P|}{|C|}$ with minimal loss of information ϵ , thus ensuring that the reconstructed point cloud P' closely approximates P ($d(P, P') \leq \epsilon$). Compression algorithms are applied in applications like autonomous driving, virtual reality, and geographic information systems, where large volumes of 3D data need to be processed and transmitted efficiently.

B. Further related work

This section provides an overview of additional point cloud compression methods that have been proposed in the literature.

B.1. Traditional point cloud compression

Some of the most commonly used traditional point cloud compression algorithms include *MPEG PCC* [34] and *AVS PCC* [22]. *MPEG PCC* is a standardization effort by the *Moving Picture Experts Group* (MPEG) for point cloud compression. *AVS PCC* is a similar standardization effort by the *Audio Video Coding Standard Workgroup of China* (AVS). Traditional point cloud compression algorithms are based on geometry coding, attribute coding, and entropy coding techniques. Yu et al. [41] propose a regularized projection algorithm to construct a reliable prediction relationship in the predictive structure. A simplified geometry pre-

diction technique is proposed based on the regularized projection pattern. [33] introduces two new encoding methods for point cloud compression, namely *Alternate Depth Compression* (ADC) and *Log-Polar* (LP). In [25] the authors propose *SCP*, a model-agnostic spherical coordinate-based point cloud compression method. Moreover, a multi-level Octree is introduced to mitigate the reconstruction error for distant areas in the point cloud.

B.2. Learning based compression

Learning-based point cloud compression algorithms have shown promising results in terms of compression efficiency and reconstruction quality. *EHEM* [35] proposes a hierarchical attention structure that has a linear complexity to the context scale and maintains the global receptive field. Furthermore, a grouped context structure is presented to address the serial decoding issue caused by the auto-regression mechanism. *PIVOT-Net* [28] introduces a heterogeneous point cloud compression framework that unifies typical point cloud representations such as point-based, voxel-based, and tree-based representations. This allows compressing point clouds at different bit-depth levels. *SparsePCGC* [38] is a sparse point cloud geometry compression method that only performs convolutions on sparsely distributed most-probable positively occupied voxels.

C. Implementation details

This section provides additional implementation details of our point cloud compression framework *PointCompress3D*.

C.1. Hardware and software setup

We run our compression framework on a GPU cluster with an AMD EPYC 7001 series CPU, 128 GB of RAM, and 3 x NVIDIA RTX 3090 GPUs. The framework runs in a Docker container based on the Ubuntu 20.04 operating system and is implemented in Python.

C.2. Parameter tuning

We perform parameter tuning to optimize the performance of our point cloud compression framework. The parameters include the grid size, the max. number of points, min. kernel size, kernel radius (encoding/decoding), quantization bits and compression level. We use grid search to find the optimal parameters for each model. The parameters are tuned on the *TUMTraf-I* dataset and are then used for testing the models on the *TUMTraf-V2X* dataset.

D. Point Cloud Compression Datasets

This section provides an overview of the most commonly used point cloud datasets for evaluating point cloud com-

pression algorithms [22].

1. **KITTI** [13]: Contains point clouds captured by a *Velo-dyne* LiDAR sensor mounted on a moving vehicle.
2. **ShapeNet** [7]: Consists of 3D models from various categories, including cars, chairs, and tables.
3. **ModelNet40** [40]: Contains 3D models from 40 categories, such as airplanes, chairs, and tables.
4. **SemanticKITTI** [5]: A large-scale dataset of point clouds with semantic annotations.
5. **TUMTraf-I** [45]: Contains point clouds captured by two Ouster LiDAR sensors mounted on roadside infrastructure.

E. Metrics

The metrics for evaluating point cloud compression performance and reconstruction quality can be categorized into performance metrics and quality metrics [33].

E.1. Performance metrics

1. Bit per point (BPP): Measures the size in bits used to represent a single point.
2. Bit-rate (BR): Total size of the computed frames divided by the frame transmission rate.
3. Compression ratio (CR): Ratio between the *BPP* of the raw point cloud and the *BPP* of the encoded point cloud.
4. Encoding and decoding time (ET, DT): Time taken to process the data and generate the corresponding output.

E.2. Quality metrics

1. Peak Signal-to-Noise Ratio (PSNR):
 - PSNR-D1: Intra-point MSE error calculated between the original and reconstructed point cloud.
 - PSNR-D2: Similar to PSNR-D1 but measures distances with respect to a plane.
2. PointSSIM (PSSIM): Measures perceptual degradations of point cloud data using statistical dispersion measurements for attributes such as colors and geometry.
3. Video Quality Assessment Point Cloud (VQA-PC): Uses spatial and temporal features extracted from a point cloud to estimate quality levels through a machine learning model.

4. Multi-Modal Point Cloud Quality Assessment (MM-PCQA): The point cloud is split into various 3D sub-models and rendered into 2D image projections. These projections are encoded with neural networks, and the quality level is estimated through a quality regression block.

These metrics are used to evaluate both the efficiency of the compression process and the quality of the reconstructed point cloud.

F. Detailed visualization results

We provide additional qualitative results of the point cloud reconstruction process using *Depoco* on the *TUMTraf-A9* and *TUMTraf-I* datasets. Figure 11 shows the original and the reconstructed point cloud on the A9 Highway with a truck and a van. Moreover, we show the original and reconstructed point cloud at an intersection showing a pedestrian and a car. These results demonstrate the effectiveness of *Depoco* in reconstructing point clouds with different objects and scenes in the *TUMTraf* datasets.

G. Failure cases and limitations

G.1. Failure cases

Learning-based point cloud compression algorithms like *3DPCC* [4] can encounter several failure cases. These include overfitting to the training data, resulting in poor performance on unseen data, and underfitting, where the model fails to capture underlying patterns. They may also struggle with data imbalance, performing poorly when one class is overrepresented, and with outliers, which can negatively impact the model’s performance on datasets that contain atypical data points.

G.2. Limitations

Depoco [39] is no longer state-of-the-art (SOTA) and has only been evaluated on the *SemanticKITTI* dataset. It is outperformed by *Draco* on the *TUMTraf-I* dataset and does not consider the compression of point attributes. Similarly, *3DPCC* [4] also does not consider the compression of attributes except the intensity and XYZ coordinates. It requires calibration data, range images, and azimuth maps for training, which are not always available in practice. It is also outperformed by *Draco* [12] on *TUMTraf-I* and is prone to overfitting. Finally, *Draco* is not as efficient as *3DPCC* or *Depoco* in terms of decoding point clouds.

References

- [1] Tinyjpg - compress jpeg images intelligently.
- [2] Siddharth Agarwal, Ankit Vora, Gaurav Pandey, Wayne Williams, Helen Kourous, and James McBride. Ford multi-av seasonal dataset. *The Int. Journal of Robotics Research*, 39(12):1367–1376, 2020.
- [3] Anique Akhtar, Zhu Li, and Geert Van der Auwera. Inter-frame compression for dynamic point cloud geometry coding. *IEEE Trans. on Image Processing*, 2024.
- [4] Till Beemelmans, Yuchen Tao, Bastian Lampe, Lennart Reiher, Raphael van Kempen, Timo Wopen, and Lutz Eckstein. 3d point cloud compression with recurrent neural network and image compression methods. In *2022 IEEE Intelligent Vehicles Symposium (IV)*, pages 345–351. IEEE, 2022.
- [5] Jens Behley, Martin Garbade, Andres Milioto, Jan Quenzel, Sven Behnke, Cyrill Stachniss, and Jurgen Gall. Semantickitti: A dataset for semantic scene understanding of lidar sequences. In *Proc. of IEEE/CVF int. conf. on computer vision*, pages 9297–9307, 2019.
- [6] Sourav Biswas, Jerry Liu, Kelvin Wong, Shenlong Wang, and Raquel Urtasun. Muscle: Multi sweep compression of lidar using deep entropy models. *Adv. in Neural Information Processing Systems*, 33:22170–22181, 2020.
- [7] Angel X. Chang, Thomas A. Funkhouser, Leonidas J. Guibas, Pat Hanrahan, Qi-Xing Huang, Zimo Li, Silvio Savarese, Manolis Savva, Shuran Song, Hao Su, Jianxiong Xiao, Li Yi, and Fisher Yu. Shapenet: An information-rich 3d model repository. *CoRR*, abs/1512.03012, 2015.
- [8] Christian Creß, Walter Zimmer, Leah Strand, Maximilian Fortkord, Siyi Dai, Venkatnarayanan Lakshminarasimhan, and Alois Knoll. A9-dataset: Multi-sensor infrastructure-based dataset for mobility research. In *2022 IEEE Intelligent Vehicles Symposium (IV)*, pages 965–970. IEEE, 2022.
- [9] Christian Creß, Walter Zimmer, Nils Purschke, Bach Ngoc Doan, Sven Kirchner, Venkatnarayanan Lakshminarasimhan, Leah Strand, and Alois C. Knoll. Tumtraf event: Calibration and fusion resulting in a dataset for roadside event-based and rgb cameras. *IEEE Transactions on Intelligent Vehicles*, pages 1–19, 2024.
- [10] Mingyue Cui, Junhua Long, Mingjian Feng, Boyang Li, and Huang Kai. Octformer: Efficient octree-based transformer for point cloud compression with local enhancement. In *Proc. of AAAI Conf. on Artificial Intellig.*, volume 37, pages 470–478, 2023.
- [11] Chunyang Fu, Ge Li, Rui Song, Wei Gao, and Shan Liu. Octtattention: Octree-based large-scale contexts model for point cloud compression. In *Proc. of AAAI conf. on artificial intellig.*, volume 36, pages 625–633, 2022.
- [12] Frank Galligan, Michael Hemmer, Ondrej Stava, Fan Zhang, and Jamieson Brett. Google/draco: a library for compressing and decompressing 3d geometric meshes and point clouds. <https://github.com/google/draco>, 2018.
- [13] A Geiger, P Lenz, C Stiller, and R Urtasun. Vision meets robotics: The KITTI dataset. 32(11):1231–1237. Publisher: SAGE Publications Ltd STM.
- [14] Ahmed Ghita, Bjørk Antoniusen, Walter Zimmer, Ross Greer, Christian Creß, Andreas Møgelmoose, Mohan M Trivedi, and Alois C Knoll. Activeanno3d—an active learning framework for multi-modal 3d object detection. In *2024 IEEE Intelligent Vehicles Symposium, IV 2024, Korea, June 2-6, 2024*, page 8. IEEE, 2024.
- [15] Yun He, Xinlin Ren, Danhang Tang, Yinda Zhang, Xiangyang Xue, and Yanwei Fu. Density-preserving deep point cloud compression. In *Proc. of IEEE/CVF Conf. on Computer Vision and Pattern Recognition*, pages 2333–2342, 2022.
- [16] Aral Hekimoglu, Philipp Friedrich, Walter Zimmer, Michael Schmidt, Alvaro Marcos-Ramiro, and Alois Knoll. Multi-task consistency for active learning. In *Proc. of IEEE/CVF Int. Conf. on Comp. Vision*, 2023.
- [17] Hamidreza Houshiar and Andreas Nüchter. 3d point cloud compression using conventional image compression for efficient data transmission. In *2015 XXV int. conf. on information, communication and automation technologies (ICAT)*, pages 1–8. IEEE, 2015.
- [18] Lila Huang, Shenlong Wang, Kelvin Wong, Jerry Liu, and Raquel Urtasun. Octsqueeze: Octree-structured entropy model for lidar compression. In *Proc. of IEEE/CVF conf. on computer vision and pattern recognition*, 2020.
- [19] Alireza Javaheri, Catarina Brites, Fernando Pereira, and João Ascenso. Improving psnr-based quality metrics performance for point cloud geometry. In *2020 IEEE International Conference on Image Processing (ICIP)*, pages 3438–3442. ISSN: 2381-8549.
- [20] Seung Lab. DracoPy: Python bindings for Draco. <https://github.com/seung-lab/DracoPy>, Accessed: 2024-05-01.
- [21] Alex H Lang, Sourabh Vora, Holger Caesar, Lubing Zhou, Jiong Yang, and Oscar Beijbom. Pointpillars: Fast encoders for object detection from point clouds. In *Proc. of IEEE/CVF conf. on computer vision and pattern recognition*, pages 12697–12705, 2019.
- [22] Ge Li, Wei Gao, and Wen Gao. *Point Cloud Compression: Technologies and Standardization*. Springer Nature.
- [23] Yingwei Li, Adams Wei Yu, Tianjian Meng, Ben Caine, Jiquan Ngiam, Daiyi Peng, Junyang Shen, Yifeng Lu, Denny Zhou, Quoc V Le, et al. Deepfusion: Lidar-camera deep fusion for multi-modal 3d object detection. In *Proc. of IEEE/CVF Conf. on Computer Vision and Pattern Recognition*, pages 17182–17191, 2022.
- [24] Mingyu Liu, Ekim Yurtsever, Jonathan Fossaert, Xingcheng Zhou, Walter Zimmer, Yuning Cui, Bare Luka Zagar, and Alois C. Knoll. A survey on autonomous driving datasets: Statistics, annotation quality, and a future outlook. *IEEE Transactions on Intelligent Vehicles*, pages 1–29, 2024.
- [25] Ao Luo, Linxin Song, Keisuke Nonaka, Kyohei Unno, Heming Sun, Masayuki Goto, and Jiro Katto. SCP: Spherical-coordinate-based learned point cloud compression. 38(4):3954–3962. Number: 4.
- [26] Gledson Melotti, Cristiano Premevida, and Nuno Gonçalves. Multimodal deep-learning for object recognition combining camera and lidar data. In *2020 IEEE Int. Conf. on Autonomous Robot Systems and Competitions (ICARSC)*, pages 177–182. IEEE, 2020.

- [27] Dat Thanh Nguyen, Maurice Quach, Giuseppe Valenzise, and Pierre Duhamel. Learning-based lossless compression of 3d point cloud geometry. In *ICASSP 2021-2021 IEEE Int. Conf. on Acoustics, Speech and Signal Processing (ICASSP)*, pages 4220–4224. IEEE, 2021.
- [28] Jiahao Pang, Kevin Bui, and Dong Tian. PIVOT-net: Heterogeneous point-voxel-tree-based framework for point cloud compression. pages 1270–1279. IEEE Computer Society.
- [29] Jiahao Pang, Kevin Bui, and Dong Tian. Pivot-net: Heterogeneous point-voxel-tree-based framework for point cloud compression. *arXiv preprint arXiv:2402.07243*, 2024.
- [30] Jiahao Pang, Muhammad Asad Lodhi, and Dong Tian. Grasp-net: Geometric residual analysis and synthesis for point cloud compression. In *Proc. of Workshop on Advances in Point Cloud Compression, Processing and Analysis*, pages 11–19, 2022.
- [31] Maurice Quach, Jiahao Pang, Dong Tian, Giuseppe Valenzise, and Frédéric Dufaux. Survey on deep learning-based point cloud compression. *Frontiers in Signal Processing*, 2:846972, 2022.
- [32] Zizheng Que, Guo Lu, and Dong Xu. Voxelcontext-net: An octree based framework for point cloud compression. In *Proc. of IEEE/CVF Conf. on Computer Vision and Pattern Recognition*, pages 6042–6051, 2021.
- [33] Pietro Rui, Lorenzo Mascia, and Enrico Grosso. Saliency-guided point cloud compression for 3d live reconstruction. 8(5):36. Number: 5 Publisher: Multidisciplinary Digital Publishing Institute.
- [34] Sebastian Schwarz, Marius Preda, Vittorio Baroncini, Madhukar Budagavi, Pablo Cesar, Philip A Chou, Robert A Cohen, Maja Krivokuća, Sébastien Lasserre, Zhu Li, et al. Emerging mpeg standards for point cloud compression. *IEEE Journal Emerging and Selected Topics in Circuits and Systems*, 9:133–148, 2018.
- [35] Rui Song, Chunyang Fu, Shan Liu, and Ge Li. Efficient hierarchical entropy model for learned point cloud compression. pages 14368–14377.
- [36] Maxim Tatarchenko, Alexey Dosovitskiy, and Thomas Brox. Octree generating networks: Efficient convolutional architectures for high-resolution 3d outputs. In *Proc. of IEEE int. conf. on computer vision*, 2017.
- [37] George Toderici, Damien Vincent, Nick Johnston, Sung Jin Hwang, David Minnen, Joel Shor, and Michele Covell. Full resolution image compression with recurrent neural networks. In *Proc. of IEEE conf. on Computer Vision and Pattern Recognition*, pages 5306–5314, 2017.
- [38] Jianqiang Wang, Dandan Ding, Zhu Li, Xiaoxing Feng, Chuntong Cao, and Zhan Ma. Sparse tensor-based multi-scale representation for point cloud geometry compression. 45(7):9055–9071. Conference Name: IEEE Transactions on Pattern Analysis and Machine Intelligence.
- [39] Louis Wiesmann, Andres Milioto, Xieyuanli Chen, Cyrill Stachniss, and Jens Behley. Deep compression for dense point cloud maps. *IEEE Robotics and Automation Letters*, 6(2):2060–2067, 2021.
- [40] Zhirong Wu, Shuran Song, Aditya Khosla, Fisher Yu, Linguang Zhang, Xiaoou Tang, and Jianxiong Xiao. 3d shapenets: A deep representation for volumetric shapes. In *Proceedings of the IEEE conference on computer vision and pattern recognition*, pages 1912–1920, 2015.
- [41] Youguang Yu, Wei Zhang, Ge Li, and Fuzheng Yang. A regularized projection-based geometry compression scheme for LiDAR point cloud. 33(3):1427–1437. Conference Name: IEEE Transactions on Circuits and Systems for Video Technology.
- [42] Xingcheng Zhou, Mingyu Liu, Bare Luka Zagar, Ekim Yurtsever, and Alois C Knoll. Vision language models in autonomous driving and intelligent transportation systems. *arXiv preprint arXiv:2310.14414*, 2023.
- [43] Xuanyu Zhou, Charles R Qi, Yin Zhou, and Dragomir Anguelov. Riddle: Lidar data compression with range image deep delta encoding. In *Proc. of IEEE/CVF Conf. on Computer Vision and Pattern Recognition*, pages 17212–17221, 2022.
- [44] Walter Zimmer, Joseph Birkner, Marcel Brucker, Huu Tung Nguyen, Stefan Petrovski, Bohan Wang, and Alois C. Knoll. Infradet3d: Multi-modal 3d object detection based on road-side infrastructure camera and lidar sensors. In *2023 IEEE Intelligent Vehicles Symposium (IV)*. IEEE, 2023.
- [45] Walter Zimmer, Christian Creß, Huu Tung Nguyen, and Alois C Knoll. Tumtraf intersection dataset: All you need for urban 3d camera-lidar roadside perception. In *2023 IEEE 26th Int. Conf. on Intelligent Transportation Systems (ITSC)*, pages 1030–1037. IEEE, 2023.
- [46] Walter Zimmer, Emec Ercelik, Xingcheng Zhou, Xavier Jair Diaz Ortiz, and Alois Knoll. A survey of robust 3d object detection methods in point clouds. *arXiv preprint arXiv:2204.00106*, 2022.
- [47] Walter Zimmer, Marcus Grabler, and Alois Knoll. Real-time and robust 3d object detection within road-side lidars using domain adaptation. *arXiv preprint arXiv:2204.00132*, 2022.
- [48] Walter Zimmer, Akshay Rangesh, and Mohan Trivedi. 3d bat: A semi-automatic, web-based 3d annotation toolbox for full-surround, multi-modal data streams. In *2019 IEEE Intelligent Vehicles Symposium (IV)*, pages 1816–1821. IEEE, 2019.
- [49] Walter Zimmer, Gerhard Arya Wardana, Suren Sritharan, Xingcheng Zhou, Rui Song, and Alois C Knoll. Tumtraf v2x cooperative perception dataset. In *Proc. of IEEE/CVF Conf. on Comp. Vision and Pattern Recog.*, page 10, 2024.
- [50] Walter Zimmer, Jialong Wu, Xingcheng Zhou, and Alois C Knoll. Real-time and robust 3d object detection with road-side lidars. In *Proc. of Int. Scientific Conf. on Mobility and Transport: Mobility Innovations for Growing Megacities*, pages 199–219. Springer, 2023.